

Analysis of a long-duration AR throughout five solar rotations: Magnetic properties and ejective events

Francisco A. Iglesias^{a,b,*}, Hebe Cremades^{a,b}, Luciano A. Merenda^a, Cristina H. Mandrini^{c,d}, Fernando M. López^e, Marcelo C. López Fuentes^c, Ignacio Ugarte-Urra^f

^a*Universidad Tecnológica Nacional – Facultad Regional Mendoza, CEDS, Rodríguez 243, 5500, Mendoza, Argentina*

^b*Consejo Nacional de Investigaciones Científicas y Técnicas (CONICET), Godoy Cruz 2290, C1425FQB, Buenos Aires, Argentina*

^c*Instituto de Astronomía y Física del Espacio (IAFE, UBA-CONICET), CC. 67, Suc. 28, Buenos Aires, 1428, Argentina*

^d*Facultad de Ciencias Exactas y Naturales (FCEN), Universidad de Buenos Aires (UBA), Intendente Guiraldes 2160, C1428EGA, Buenos Aires, Argentina*

^e*Instituto de Ciencias Astronómicas, de la Tierra y del Espacio (ICATE), CONICET-UNSJ, Av. Espaa 1512 sur, 5400, San Juan, Argentina*

^f*Space Science Division, Naval Research Laboratory, 4555 Overlook Ave SW, Washington DC, 20375, USA*

Abstract

Coronal mass ejections (CMEs), which are among the most magnificent solar eruptions, are a major driver of space weather and can thus affect diverse human technologies. Different processes have been proposed to explain the initiation and release of CMEs from solar active regions (ARs), without reaching consensus on which is the predominant scenario, and thus rendering impossible to accurately predict when a CME is going to erupt from a given AR. To investigate AR magnetic properties that favor CMEs production, we employ multi-spacecraft data to analyze a long duration AR (NOAA 11089, 11100, 11106, 11112 and 11121) throughout its complete lifetime, spanning

*Corresponding author

Email addresses: franciscoiglesias@frm.utn.edu.ar (Francisco A. Iglesias), hebe.cremades@frm.utn.edu.ar (Hebe Cremades), lucianomerenda3@gmail.com (Luciano A. Merenda), mandrini@iafe.uba.ar (Cristina H. Mandrini), fmlopez@conicet.gov.ar (Fernando M. López), lopezf@iafe.uba.ar (Marcelo C. López Fuentes), ignacio.ugarte-urra@nrl.navy.mil (Ignacio Ugarte-Urra)

five Carrington rotations from July to November 2010. We use data from the Solar Dynamics Observatory to study the evolution of the AR magnetic properties during the five near-side passages, and a proxy to follow the magnetic flux changes when no magnetograms are available, i.e. during far-side transits. The ejectivity is studied by characterizing the angular widths, speeds and masses of 108 CMEs that we associated to the AR, when examining a 124-day period. Such an ejectivity tracking was possible thanks to the multi-viewpoint images provided by the Solar-Terrestrial Relations Observatory and Solar and Heliospheric Observatory in a quasi-quadrature configuration. We also inspected the X-ray flares registered by the GOES satellite and found 162 to be associated to the AR under study. Given the substantial number of ejections studied, we use a statistical approach instead of a single-event analysis. We found three well defined periods of very high CMEs activity and two periods with no mass ejections that are preceded or accompanied by characteristic changes in the AR magnetic flux, free magnetic energy and/or presence of electric currents. Our large sample of CMEs and long term study of a single AR, provide further evidence relating AR magnetic activity to CME and Flare production.

Keywords: Sun: activity, Sun: coronal mass ejections (CMEs), Sun: photosphere, Sun: magnetic fields

1. Introduction

Active regions (ARs) are areas of intense magnetic field concentration on the Sun that are constantly evolving throughout their lifetime, typically ranging from days to a few months (see e.g. [van Driel-Gesztelyi and Green 2015](#) and references therein). From their generation, linked to the emergence and concentration of new photospheric magnetic flux, to their decay, partially driven by the spatial spreading and cancellation of such flux, ARs are centers of diverse magnetic activity. They provide vital constraints to model the underlying dynamo process ([van Driel-Gesztelyi and Green, 2015](#)) and are also the main source region of different kinds of transient phenomena, such as solar flares (see e.g. [Priest and Forbes 2002](#)) and coronal mass ejections (CMEs). CMEs involve the fast release of large amounts of mass and magnetic field from the solar corona into the interplanetary medium (sometimes exceeding 2500 km s^{-1} and 10^{16} g), see e.g. [Webb and Howard 2012](#). They produce significant perturbations in the solar wind and can strongly

influence the geomagnetic environment conditions, a.k.a space weather, see e.g. [Bothmer and Daglis \(2007\)](#) and [Zhang et al. \(2018\)](#).

Magnetic energy dominates other forms of energy in the low corona, particularly near ARs, where magnetic pressure overcomes plasma pressure and drives the matter dynamics. The occurrence of a CME is then of magnetic nature, as summarized in [Green et al. \(2018\)](#) requiring (a) the previous build-up of free magnetic energy stored in the non-potential core field, which may or may not contain a filament and is generally located above the polarity inversion line (PIL) of ARs; (b) a destabilizing mechanism that triggers the eruption of the core field; and (c) a driving mechanism that powers the ejection of the core field from the low to the high corona while interacting with the overlying strapping field.

Several mechanisms contribute to build up non-potential energy and magnetic helicity in the coronal field associated to ARs. These include, among others, sunspot rotation, the frequent emergence of twisted magnetic flux tubes (or flux ropes, see e.g. [Hood et al. 2009](#); [Poisson et al. 2015a](#)) and the stress produced in the field lines by shearing photospheric flows (e.g. [MacTaggart and Hood, 2010](#)). There is substantial observational evidence of the presence in the solar atmosphere of the topological features (e.g. S-shaped loops, magnetic tongues, etc.) and electric currents associated to such a non-potential field, e.g. [Rust and Kumar \(1996\)](#); [McKenzie and Canfield \(2008\)](#); [Koleva et al. \(2012\)](#); [Jiang et al. \(2014\)](#); [Poisson et al. \(2015b\)](#). Abrupt magnetic reconfigurations, associated to the reconnection of field lines, transform large amounts of the free magnetic energy stored in the coronal field into kinetic and thermal energy, powering eruptive events such as CMEs and flares, e.g. ([Kliem et al., 2014](#); [Aulanier et al., 2010](#)).

CMEs are commonly associated with flux rope eruptions, e.g. [Li et al. \(2012\)](#); [Jiang et al. \(2014\)](#); [Vourlidas et al. \(2013\)](#). Different mechanisms have been proposed and evidenced in the literature to explain CME triggering, including flux emergence (e.g. [Chen et al. 1997](#) and [Manchester et al. 2004](#)), reconnection of field lines below (tether-cutting model, [Moore and Roumeliotis 1992](#)) or above (breakout model, [Antiochos et al. 1999](#)) the flux rope, excess of twist in the flux rope (kink instability, [Török and Kliem 2005](#)) and others (e.g. [Amari et al. 2000](#); [Lin et al. 2004](#) and [Aulanier et al. 2010](#)).

Once the core field is destabilized, it rises stretching and pushing aside the overlying coronal field. It can be the case that this strapping field restrains the rising core field, preventing its ejection and producing a confined CME, see e.g. [Török and Kliem \(2005\)](#) and [Moore et al. \(2001\)](#). In any

case, the above-named trigger mechanisms are not able to explain the observed acceleration and expansion of CMEs in the low corona. Instead, two driving processes have been proposed, namely the torus instability (a.k.a. flux-rope catastrophe model, e.g. [Kliem and Török, 2006](#); [Aulanier et al., 2010](#)), which occurs when the outward magnetic pressure of the flux rope exceeds the inward magnetic tension provided by the external field; and the flare-reconnection (e.g. [Forbes et al., 2018](#)), that describes the successive magnetic reconnections occurring at the vertical current sheet formed below the rising core field, and its associated flaring activity.

Mainly due to the lack of routine magnetic field measurements of the corona, no clear consensus has been reached regarding which of the named trigger and driving mechanisms, or what combination of them, is the predominant, see e.g. the discussions in [Webb and Howard \(2012\)](#); [Green et al. \(2018\)](#). Moreover, the activity of ARs varies during their lifetime. Flares are common in the emergence and stable phase, decreasing in number with the reduction of flux density during decay. On the other hand, CME production is generally low during the emergence of young ARs, however, it can persist or even increase during the stable and decay phases, see Sect. 4 and e.g. [Li et al. \(2012\)](#); [Démoulin et al. \(2002\)](#). Because of this, studying the evolution of the magnetic properties of ARs in connection with their associated eruptive events is an active area of research. The vast literature includes short-term (a fraction of the AR lifetime), detailed analyses focusing on, e.g. comparative CME-production (e.g. [Cremades et al. 2015](#); [Murray et al. 2018](#)), pre- and post-eruptive coronal magnetic field topology (e.g. [Mandrini et al. 2014, 2006](#); [Chandra et al. 2011, 2017](#)) and magnetic helicity evolution (e.g. [Romano et al. 2014](#); [Démoulin et al. 2002](#); [Mandrini et al. 2004](#)). There are also investigations of the long-term (time scales covering a full AR lifetime or more) evolution of, e.g. the magnetic influence of AR plasma flows (e.g. [Harra et al. 2017](#); [Zangrilli and Poletto 2016](#) and [Ko et al. 2016](#)), the CME production rate along the solar cycle (e.g. [Gopalswamy et al. 2003](#) and [Riley et al. 2006](#)), the global magnetic field and its associated CME production ([Petrie, 2013](#)), and the continuous tracking of some AR magnetic properties (e.g. [Démoulin et al. 2002](#) and [Green et al. 2002](#)), among many others, see e.g. the review by [van Driel-Gesztelyi and Green \(2015\)](#).

Given the present fleet of Sun-observing missions, up to date we can only obtain magnetograms of the portion of the solar surface that is facing Earth, i.e. the near side. Moreover, limb darkening and spherical effects harm the quality of the magnetograms obtained from a fixed Earth perspective, e.g. the

noise properties of the tangential and radial field components change from disk center to the limb. Therefore, all long-term studies cited above were either done on ARs that live less than approximately half a solar rotation, are restricted to only the intervals where the AR is on the near side, or have used a proxy to estimate magnetic properties when the AR is on the far side, such as using 304 Å intensity images or constrained magnetic surface flux transport models to estimate total flux, see e.g. [Ugarte-Urra et al. \(2015\)](#). On the contrary, the above-named limiting factor is not present when studying the CME production of an AR. There is the possibility of continuous tracking of the CME production of an AR using a combination Sun-observing spacecraft such as SDO (Solar Dynamics Observatory; [Pesnell et al. 2012](#)) and/or SOHO (Solar and Heliospheric Observatory; [Domingo et al. 1995](#)) plus the two STEREO (Solar-Terrestrial Relations Observatory; [Kaiser et al. 2008](#)), provided that the latter are favorably located so as to track the AR during its far side passage, i.e. nearly in quadrature with the Sun-Earth line ($\approx 180^\circ$ apart). This combination of observatories offers a unique opportunity to examine the CME production continuously during one or more full solar rotations.

The present work reports on the CME and X-ray flare production of a long duration AR (NOAA 11089, 11100, 11106, 11112 and 11121) throughout its complete lifetime, spanning five Carrington rotations (CRs) from July to November 2010. We also analyze the evolution of some of the AR photospheric magnetic properties (magnetic flux, current helicity and a proxy of the photospheric free magnetic energy, see Sect. 2.1 for exact definitions) to study their relationship with the frequency and properties of the ensued CMEs. Given the substantial number of mass ejections studied (108) and their clustering in bursts, we do not focus on single events but relate the long-term (few days) variation of the AR magnetic properties to the occurrence of bursts of CMEs, i.e. high CME activity periods. The rest of this work is organized as follows. Section 2 presents the methodology and analyzed data, including that of the AR (Sect. 2.1) acquired during its near-side (using HMI and AIA¹ onboard SDO, and MDI² onboard SOHO) and far-side

¹The Helioseismic and Magnetic Imager (HMI, [Scherrer et al. 2012](#)) and the Atmospheric Imaging Assembly (AIA, [Lemen et al. 2012](#)) are both onboard the SDO spacecraft (in geosynchronous orbit).

²The Michelson Doppler Imager (MDI, [Scherrer et al. 1995](#)) onboard the SOHO spacecraft (located at Lagrangian point 1 of the Sun-Earth system).

(using SECCHI EUVIs³ onboard STEREO) transits. Sect. 2.2 describes the SECCHI and LASCO⁴ data that allowed us to track the AR, identify its associated CMEs and derive their main properties. Sect. 2.3 introduces the Geostationary Operational Environmental Satellite (GOES) data used to identify X-ray flares originating in the AR. Sect. 3 presents and describes the resulting time series that drive the discussion and conclusions given in Sect. 4.

2. Data sets and methodology

After Solar Cycle 23, a long solar minimum of over two years, and more than 800 days without sunspots, a series of long-duration ARs emerged on the Sun. Many of these had strong magnetic activity with flares, filament eruptions and CMEs, see e.g. Schrijver et al. (2011); Liu et al. (2012); Li et al. (2012); Mandrini et al. (2014).

The inspected AR was born in the far side of the Sun and appeared for the first time on the east limb as NOAA AR 11089 on 19 July 2010, persisting for approximately five CRs until mid-November 2010. During that period, the STEREO twin spacecraft were approaching a quadrature configuration with respect to Earth, i.e. they were $\approx 148^\circ$ and $\approx 168^\circ$ apart at the beginning and end of the mentioned time interval, respectively. At the same time, the SDO mission was beginning its operational phase, providing views of the AR from Earth’s perspective. Numerous episodes of flux emergence and ejective activity were observed during the lifetime of the investigated AR. As a consequence, it has been subject of independent, short-term studies that address different aspects and stages of its evolution, e.g. Guo et al. (2013); Zuccarello et al. (2014); Mandrini et al. (2014); Cremades et al. (2015). In the latter two articles, AR 11121 is analyzed together with the closely related AR 11123, which emerged within AR 11121 during November 2010.

The photospheric imprints of the inspected AR can be seen in Fig. 1, which presents the line-of-sight magnetograms during its five central meridian passages. We also display the different NOAA numbers that were assigned

³The Extreme-Ultraviolet Imagers (EUVIs) are part of the Sun–Earth Connection Coronal and Heliospheric Investigation experiment (SECCHI, Howard et al. 2008) onboard of the two STEREO spacecrafts (orbiting the sun in opposite directions).

⁴The Large-Angle and Spectrometric Coronagraph Experiment (LASCO, Brueckner et al. 1995) onboard the SOHO spacecraft.

to the AR after each new solar rotation, together with the dates at which it appeared on the east limb, was at central meridian, and disappeared on the west limb. The AR is seen to constantly evolve, starting with a configuration predominantly formed by two bipoles in CR 2099 (top-left panel in Fig. 1). During the near-side transit of the AR the bipoles do not present strong photospheric interaction, e.g. cancellation of opposite polarities, and the western, weaker bipole diffuses to be absent in CR2100. Moreover, we did not find obvious signs of coronal magnetic interaction (in terms of simultaneous EUV brightenings occurring over both bipoles) and the CME activity was low (as is frequent in young ARs, see Sect. 1). After this, the AR adopts a predominantly bipolar configuration from CR 2100 to CR 2102. During the last rotation (CR 2103, shown in the bottom-right panel of Fig. 1) the bipolar AR 11123 emerged in the negative polarity area of the decaying AR 11121, strongly incrementing the CME activity (see Sect. 4).

In the following three subsections we describe the data sets employed to study the evolution of the photospheric magnetic field, as well as the CME and X-ray flare production along the AR lifetime.

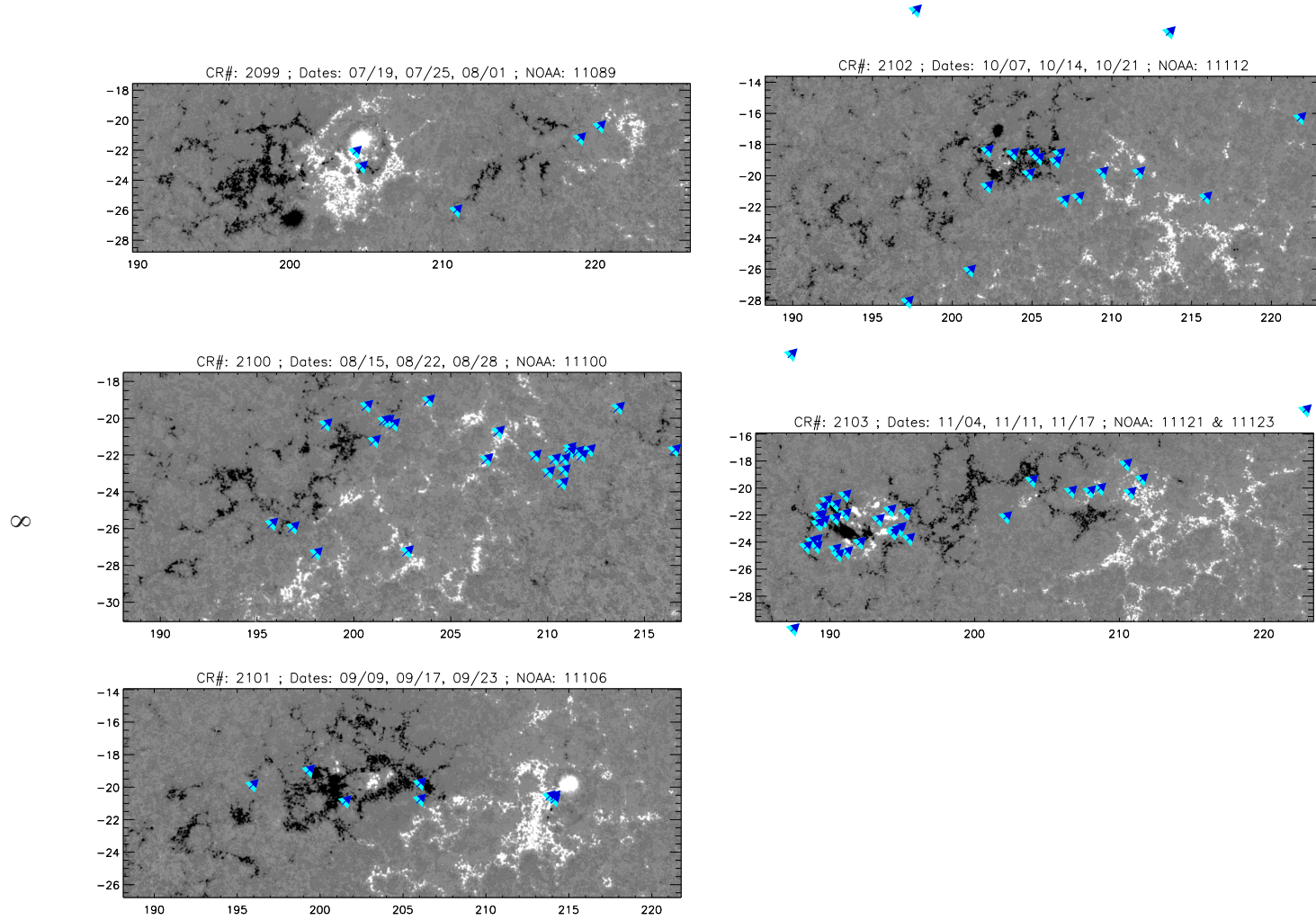


Figure 1: SHARP patches showing line-of-sight magnetograms of the investigated AR during its five central-meridian passages. The spatial scales are in degrees. The color scale ranges from -500 to 500 G with fields pointing outwards of the solar surface in white. The title of each patch gives the CR number; the dates (in the format month/day) when the region was at the west limb, central meridian and east limb; and the assigned NOAA number, respectively. The blue arrows point to the approximate location of EUV brightenings or filamentary eruptions associated to 96 CMEs that occurred at different times within each solar rotation, see Sect. 2.2 for extra details.

2.1. Photospheric properties

Magnetic flux evolution is expected to show correspondence with eruptive activity given that photospheric motions, including those related to flux emergence, have been pointed out as a possible trigger of CME eruptions, e.g. [Chen \(2011\)](#); [van Driel-Gesztelyi and Green \(2015\)](#). AR parameters characterizing the field non-potentiality, e.g. electric currents or free magnetic energy, have been also widely accepted to be related to solar eruptions, e.g. [Canfield et al. \(1999\)](#); [Falconer et al. \(2006\)](#); [Wang and Zhang \(2008\)](#); [Guo et al. \(2013\)](#); [Liu et al. \(2016\)](#). Here we analyze temporal series of the total unsigned magnetic flux ($\sum |B_z| dA$), mean current helicity ($\bar{H}c \propto \frac{1}{N} \sum B_z J_z$), total unsigned current helicity ($Hc \propto \sum |B_z J_z|$), and a proxy of the mean photospheric free magnetic energy density ($\frac{1}{N} \sum (\mathbf{B}^{obs} - \mathbf{B}^{pot})^2$), where \mathbf{B} is the magnetic field vector with radial component B_z , N is the number of spatial resolution elements (magnetogram pixels) contributing to the computation, J_z is the current density in the radial direction and dA gives the surface area covered by each pixel. In the free energy density expression, \mathbf{B}^{obs} and \mathbf{B}^{pot} represent the observed and potential field (modeled) respectively. These data series are obtained from the Space-weather HMI Active Region Patches (SHARPs; [Bobra et al. 2014](#)) during the AR near-side passages, covering 124 days (from 17 July to 18 November 2010). The SHARPs (see [Fig. 1](#)) are standard data products extracted from HMI 12 min-cadence, full-disk, vector magnetograms. Only pixels with transverse field strength that exceed the azimuth disambiguation noise threshold (≈ 150 G) contribute to the patch parameters, see [Bobra et al. \(2014\)](#) for extra details.

We additionally estimated the time evolution of the total unsigned magnetic flux in the AR using two other independent sources. The first one are full-disk, level-1.8 MDI magnetograms. These data are the average of 5 line-of-sight magnetograms with a cadence of 30 s and a noise error of 20 G per pixel. They are constructed once every 96 min and have an error in the flux density per pixel of 9 G. Following [Green et al. \(2003\)](#), to find the AR flux, a polygonal contour is fitted around the AR. The shape of the contour is given by the large gradient between the AR and the network fields. Within this region, the flux is calculated for all pixels with absolute fields above 50 G. Due to the limitations related to the projection effects involved in the magnetic flux determination, we only show values corresponding to the dates when the AR was on central meridian ± 4 days. The resulting MDI flux curves were divided by a cross-calibration factor of 1.40 to make them comparable to the HMI results, see [Liu et al. \(2012b\)](#); [Chertok et al. \(2019\)](#).

The second method employed, estimates the total unsigned magnetic flux using its strong positive correlation with the total brightness of the He II 304 Å spectral line (e.g. [Schrijver 1987](#)). We used the technique developed by [Ugarte-Urra et al. \(2015, 2018\)](#), which allows estimating the flux when magnetograms are not available, by employing intensity-only 304 Å images as a proxy. In this technique, a synchronic Carrington map covering most of the solar surface is assembled by combining quasi-simultaneous images of the 304 Å channels of the STEREO EUVIs and SDO AIA instruments. The covered solar surface depends on the SDO and STEREO spacecraft locations. The EUVI and AIA data are previously corrected to account for limb darkening effects and the time-dependent, cross-calibration of the instruments. The EUV synchronic maps allow tracking the movement of the AR on the solar surface, in our case at a cadence of one image every 6h. A fixed-sized, square box is defined around the AR of interest in each map, and the total photon flux is computed by adding the contributions of all pixels within the box that also belong to the AR. Pixels with a flux two standard deviations above the normal distribution of quiet Sun flux in full maps are considered to belong to an AR. The total photon flux can then be translated to the total unsigned magnetic flux using a known power-law relationship, see [Ugarte-Urra et al. \(2018, 2015\)](#) for extra details. This technique can be applied under complex scenarios, e.g. strong emergence within an AR as is the case of ARs 11121 and 11123. The 304-proxy method may, however, underestimate the magnetic flux when sunspots are present within the considered area. Sunspots, while contributing significant magnetic flux to active regions, do not emit strongly in coronal or chromospheric spectral lines such as those contained in the 304 Å bandpass. This caveat is already implicit in the power-law relationship which was optimized for magnetic flux densities in the range 90–900G ([Fludra and Ireland, 2008](#)). Note that, the differences between MDI and HMI spatial resolution plus the different lower-field thresholds employed in the flux estimations named above, may introduce discrepancies between their results.

2.2. CME productivity

Using quasi-simultaneous observations from multiple vantage points, we have tracked the AR in EUV wavelengths for five solar rotations and identified its productivity in terms of white-light ejecta. The nearly-quadrature observations enabled a better estimation of the ejecta source regions, a sometimes challenging task, in particular for events propagating along the Sun-

observer line (halo CMEs) which can lack structure, be diffuse and dim (see e.g. [Lara et al. 2006](#); [Cremades et al. 2015](#)). The location of the AR was decisive to determine which instrument was best to observe the region and its associated eruptive phenomena. During the AR near-side passages we examined it with AIA and HMI onboard SDO, while we detected the ensuing CMEs from a quadrature perspective using the STEREO/SECCHI COR2 coronagraph. Likewise, when the AR was close to the solar limbs (from Earth’s viewpoint), we used the SECCHI EUVIs to track the region activity (EUVI-B for the east limb and EUVI-A for the west limb), and SOHO/LASCO C2 to identify the associated mass ejections. As the AR transited the far side of the Sun, we also used the SECCHI EUVIs to monitor its behavior, while the SECCHI COR2 coronagraphs were used to detect the associated eruptions. Note that we do not use LASCO C3 or SECCHI HI data, to reduce the effects of the surrounding corona on the derived CME properties, for instance due to solar wind acceleration or mass loss.

After careful inspection of these observations, we compiled 108 CMEs that could be associated to the AR of interest, these are presented in Table 1. During this selection, we included all kinds of white-light ejecta that were discernible from the background corona in running-difference images, and at least in two consecutive images. For each CME we obtained the following properties, which are directly associated to the energy involved in the event given that generally wider CMEs are more massive and faster (see e.g. [Gopalswamy 2010](#)):

- *EUV brightening location and time*: We inspected regular and running difference images of the 171, 195 and 304 Å channels to track back the initiation of the identified CMEs using their maximum cadence (≈ 10 min). We adopted the location of the maximum brightening observed at any of these wavelengths, preferentially 304 Å. Whenever we could identify an extended structure, such as a filament as the responsible for a given CME, we took instead the coordinates of the central point of that structure. This was done to unambiguously associate the CMEs with the AR under study. Similarly, the ejection time is defined as the time of the first EUV brightening or filament eruption. Table 1 lists these ejection times, along with the time of the first appearance of the associated CME leading edge in white-light images of LASCO C2 or COR2.
- *Angular width (AW)*: The AW was measured in the set of coronagraphic

images where the CME propagation direction was closer to the corresponding plane of the sky (e.g. [Cremades et al., 2015](#)). For completeness, we also consulted the LASCO CME Catalog ([Yashiro et al., 2004](#)) and the Computer-Aided CME Tracking catalog (CACTus, [Robbrecht and Berghmans 2004](#)).

- *Mass:* The coronal electron density can be estimated from the total brightness of white-light coronagraphic images using the method introduced by [Vourlidas et al. \(2010\)](#), which makes use of the Thomson scattering properties ([Billings, 1966](#)) and assumes the electrons propagate predominantly in the plane perpendicular to the line of sight. After assuming a given plasma composition, e.g. a mixture of completely ionized hydrogen and 10% helium, the electron density can be translated to total mass, see e.g. [Colaninno and Vourlidas \(2009\)](#). Given the large number of events, we followed the implementation by [López et al. \(2017\)](#) which uses data from a single coronagraph to derive the total mass of each event, by adding the contribution of the mass associated to each pixel that belongs to the CME. The boundary of the CME is manually selected by defining a freehand region of interest.
- *Linear propagation speed:* Given that many of the selected events are not cataloged (44%), we derived their plane-of-sky propagation speed from a linear fit to height-time data points. These data points were obtained from a manual tracking of the CME leading-edge, using running-difference, coronagraphic images of LASCO C2 or SECCHI COR2 (depending on whether the direction of propagation was closer to one or the other, see below). Therefore, for accelerated or decelerated events, the speed we derived represents their mean speed in the 1.5-2 to 6 solar radii height range. The exact measurement interval within this range is event-dependent, e.g. dim CMEs could not be generally followed across the complete field of view.

Table 1: Identification numbers (ID), dates (in dd/mm format) and times of 108 white-light ejective events (CMEs), originating from the AR under study. The times in columns labeled EUV correspond to the first brightening observed in AIA or EUVI EUV images. The times in columns labeled WL correspond to the first appearance in LASCO C2 or COR2 images. We also include the class of the associated GOES X-ray flare for 33 CMEs, as a super index of the ID number. The horizontal lines delimit the beginning (thick lines) and end (thin lines) of the high CME activity periods, see Sect. 2.2.

ID	Date	EUV	WL	ID	Date	EUV	WL	ID	Date	EUV	WL	ID	Date	EUV	WL
1	19/07	09:16	10:06	28	01/09	09:45	10:24	55 ^C	18/10	16:30	17:12	82 ^B	10/11	16:45	17:24
2	20/07	06:01	07:54	29	01/09	12:00	12:36	56 ^C	19/10	07:00	07:12	83 ^C	11/11	02:15	02:54
3 ^B	20/07	09:31	10:30	30	01/09	13:30	13:54	57 ^B	19/10	12:45	14:36	84	11/11	05:15	05:39
4 ^B	23/07	12:00	13:39	31	01/09	15:10	15:24	58	19/10	16:10	16:36	85 ^C	11/11	07:30	07:54
5	02/08	16:30	17:54	32	01/09	19:15	20:08	59	19/10	18:45	19:00	86 ^B	11/11	10:15	10:39
6	05/08	00:30	01:24	33	01/09	21:45	22:08	60	19/10	23:10	23:27	87 ^C	11/11	13:15	13:39
7	08/08	00:05	08:54	34	02/09	09:10	09:39	61 ^B	20/10	01:15	01:25	88 ^C	11/11	16:15	16:39
8	10/08	04:35	05:54	35	02/09	15:30	16:08	62 ^C	20/10	11:55	12:12	89 ^C	12/11	19:30	19:54
9	15/08	05:50	06:24	36	02/09	12:00	18:54	63	21/10	23:30	23:48	90 ^B	12/11	00:15	00:24
10	18/08	01:30	03:24	37	03/09	12:45	14:54	64	22/10	01:00	01:48	91 ^C	12/11	01:45	01:54
11	21/08	14:45	15:39	38	04/09	08:10	08:24	65	22/10	05:00	05:12	92 ^C	12/11	04:00	04:24
12	23/08	12:00	23:24	39	05/09	07:45	08:24	66	23/10	01:00	01:58	93 ^C	12/11	08:10	08:24
13	27/08	11:30	10:12	40	06/09	00:05	00:24	67	23/10	04:30	05:25	94 ^B	12/11	09:15	09:24
14	28/08	16:45	17:24	41	08/09	10:30	11:00	68	28/10	11:00	11:24	95	12/11	11:45	12:24
15	30/08	04:15	05:12	42	08/09	23:45	00:24	69	28/10	16:00	17:24	96 ^C	12/11	13:45	14:08
16	30/08	07:30	08:36	43	09/09	06:00	06:48	70	29/10	12:00	04:39	97	13/11	02:00	02:54
17	30/08	14:20	15:36	44	15/09	14:10	14:39	71	29/10	12:00	18:24	98	13/11	09:30	11:08
18	30/08	17:30	18:36	45	16/09	09:00	09:39	72	31/10	10:00	11:24	99 ^C	13/11	11:45	12:24
19	30/08	19:20	19:46	46 ^B	17/09	00:15	00:39	73	02/11	09:50	10:12	100	13/11	14:15	14:38
20	30/08	22:10	23:05	47 ^B	17/09	03:45	04:54	74	03/11	02:00	02:36	101 ^C	14/11	00:00	00:24
21	31/08	00:20	01:24	48	08/10	09:10	10:24	75 ^C	03/11	06:05	06:24	102	14/11	03:15	04:24
22	31/08	02:30	03:24	49	10/10	20:03	22:24	76	03/11	09:10	09:24	103	14/11	17:30	18:24
23	31/08	05:45	06:24	50	11/10	09:00	09:44	77 ^C	03/11	12:25	12:36	104 ^B	15/11	14:45	15:24
24	31/08	12:00	14:12	51	15/10	09:45	11:24	78 ^M	05/11	14:30	15:12	105	17/11	02:30	02:47
25	31/08	19:10	20:24	52 ^M	16/10	19:30	20:24	79	06/11	01:25	03:12	106 ^B	17/11	08:15	08:23
26	31/08	20:50	21:14	53	17/10	04:00	05:00	80 ^M	06/11	15:40	16:12	107	17/11	14:25	15:11
27	01/09	06:30	07:12	54 ^C	17/10	09:00	09:36	81 ^B	10/11	14:20	14:54	108	17/11	18:20	18:35

We note that, for the computation of the AW, mass and linear speed we used the coronagraphic images where the CME propagation direction was closer to the corresponding plane of the sky, i.e. up to 45° , to reduce projection effects. The latter cannot be ruled out unless a tridimensional model or tomographic reconstruction of the CME is applied, see e.g. [Pluta et al. \(2019\)](#). However, projection errors effects are milder in our statistical approach due to the different propagation directions of the large number of CMEs analyzed.

2.3. X-ray flaring productivity

We collected the AR production of X-ray flares in the $1\text{-}8\text{ \AA}$ band by inspecting the catalog of the GOES satellite, available at <https://www.ngdc.noaa.gov/stp/solar/s>. We included all flares cataloged B-class ($10^{-7}\text{-}10^{-6}\text{ W m}^{-2}$) or superior, originating from ARs NOAA 11089, 11100, 11106, 11112, 11121 or 11123; and registered from 19 July to 17 November 2010. A total of 162 flares were found, with 127 (78%), 31 (20%) and 4 (2%) being of class B, C and M, respectively.

3. Results

Fig. 2 presents the measured properties of the 108 identified ejective events: AW, mass, speed, and occurrence rate, as a function of time. The bottom panel (number of CMEs per day) shows periods of time that stand out from the rest, in that either many CMEs occur in only few days, or no mass ejections are registered during one or more weeks. We identified five such time intervals, with two of them being no-activity periods (NAP1 and NAP2) and three of them high activity periods (HAP1, HAP2 and HAP3), see labels and vertical dotted and dashed lines in Fig. 2. Table 2 details the time intervals and relevant properties of these activity periods. Note that HAP1, HAP2 and HAP3 combined cover only 16% (20 days) of the AR lifetime (≈ 124 days) but account for 59% (64) of the total number of produced CMEs. On the other hand, NAP1 and NAP2 combined imply 23% (29 days) of the AR lifetime without a single registered CME.

The bottom panel in Fig. 2 also presents the daily frequency of the 162 GOES X-ray flares associated to the AR (red histogram). Note that, flaring activity is not available when the AR is in the far side (see the blue segments in the horizontal axis). A total of 62 CMEs were ejected during AR near-side transits; out of these, we could associate 33 to a GOES flare (13, 17 and 3

Table 2: Five CME activity periods of the AR under study. We detail various properties (Col. 1) for two no ejective activity periods, NAP1 and NAP2 (Cols. 2 and 4, respectively), three periods of high CME production, HAP1, HAP2 and HAP3 (Cols. 3, 5 and 6, respectively), and the total AR lifetime (Col. 7). The asterisk in the number of X-ray flares means that no data is available because the AR was in the far-side. For each CME property we show the temporal average and standard error. See Fig. 2 and the text for extra details.

Property	NAP1	HAP1	NAP2	HAP2	HAP3	Total
Starting date	24/07	30/08	18/09	17/10	10/11	19/07
Ending date	01/08	04/09	07/10	23/10	16/11	17/11
Duration [days]	9	6	20	7	7	124
CMEs	0	24	0	15	24	108
X-ray flares	15	*	*	23	31	162
Asoc. CME-flare	0	*	*	6	17	33
CME AW [°]	-	38±19	-	38±16	32±10	33±18
CME Mass [10^{14} g]	-	5.7±7.4	-	2.6±2.5	4.7±5.1	5.6±10.5
CME Speed [km s^{-1}]	-	514±353	-	282±110	429±205	394±235

of class B, C and M, respectively), see Table 1. This association rate implies that only 53% (33 out of 62) of the CMEs were accompanied by a flare, while 20% (33 out of 162) of the flares were related to a CME. Moreover, the more energetic the flares, the higher is the association rate with CMEs, i.e. 10% (13 out of 127) , 55% (17 out of 31), 75% (3 out of 4) of class B, C and M, respectively.

For 96 out of the 108 CMEs, we could identify the location of their associated EUV brightening. These are indicated by the blue arrows over the central-meridian magnetograms of each CR in Fig. 1. It can be seen that the brightenings are occurring in various places above the AR throughout its lifetime. During HAP1 (CR 2100), the brightening clump together either near the PIL or a small ($\approx 5^\circ$ radius) cluster in the positive polarity section. During HAP3 (CR 2103) most of the brightenings (27 out of 36) originated from AR 11123.

From the top panel in Fig. 2 and Table 2, it can be seen that the AW distribution of HAP3 is narrower than those for HAP1 and HAP2, with all CMEs having AWs below $\approx 45^\circ$. The largest AW (97°) was detected out of the high activity periods for a rather isolated CME occurring on 10 October at 20:03. Fig. 3 presents the distribution of all AWs, including their average

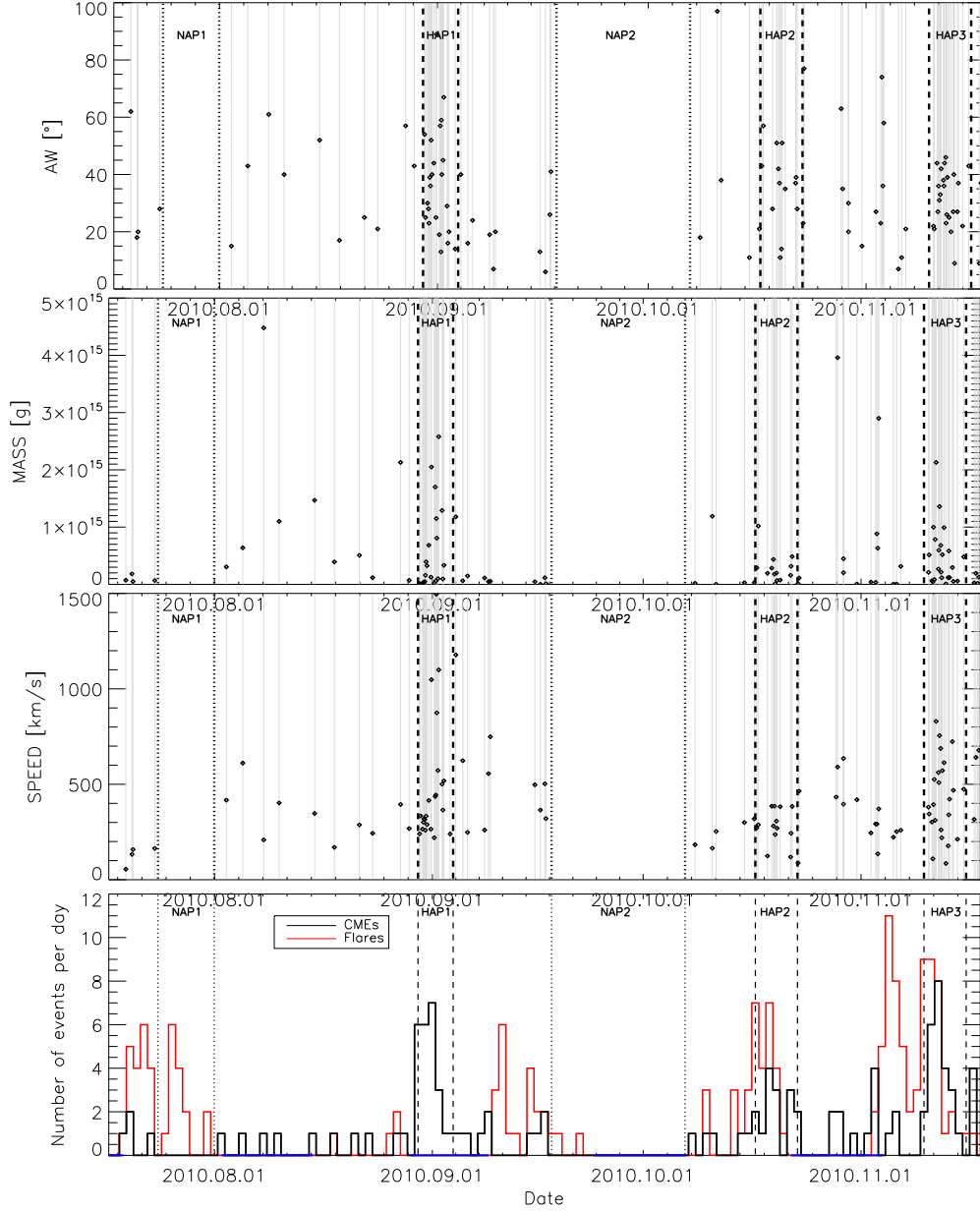


Figure 2: Time evolution of CME properties. From top to bottom we present the measured angular width, mass, linear speed and daily frequency of occurrence (black histogram), for the 108 identified CMEs. The vertical solid grey lines mark the onset of a CME. Periods of high (no) CME activity, HAP (NAP), are delimited by the vertical dashed (dotted) lines and labeled in each panel. In the bottom panel, we also indicate the time periods when the AR was in the far side (blue segments in the horizontal axis) and plot the daily frequency of GOES flares (red histogram).

($\approx 33^\circ$) and standard error ($\approx 18^\circ$). On the other hand, the distribution of all CME masses is strongly skewed (4.09) towards high values, see Fig. 3, with a mean of 5.6×10^{14} g which is slightly higher to the value reported by [Vourlidas et al. \(2010\)](#), 3.9×10^{14} g. The dispersion and mean value of the masses during HAP2 are approximately half of the values registered for HAP1, HAP3 and the full set, see Table 2. Regarding speeds, the largest were registered during HAP1, with 4 events having speeds above 1000 km s^{-1} . The dispersion and mean value of the speeds during HAP2 are also below the figures registered for HAP1, HAP3 and the full set, see Table 2. The overall speed distribution is mildly skewed towards high values (1.83) with an average ($\approx 394 \text{ km s}^{-1}$) within the slow solar wind speed range ($< 500 \text{ km s}^{-1}$, [Abbo et al. 2016](#)), see Fig. 3.

Fig. 4 shows the AR photospheric field properties for the full analyzed time interval. As explained in Sect. 2.1, HMI magnetograms and thus SHARP data are only available during the near-side passages of the AR, while HAP1 occurred when the AR was on the far side. The total unsigned flux curves derived from three different sources are plotted in the top panel of Fig. 4 with different colors. They differ from each other due to the limitations of each technique, which have been addressed in Sect. 2.1. In particular, the flux derived from the 304 \AA images underestimates the SHARP flux during the first and third near-side passages. However, the general trend of variation is similar in all three flux estimations, except during the end of the third and fifth near-side passages. The flux derived from the 304 \AA images has been interpolated and smoothed with a 24 h window, to reduce the influence of flaring activity (see [Ugarte-Urra et al. 2015](#)), and fitted with an spline to obtain an continuous estimation.

4. Discussion and conclusions

To provide further insights on the ejective activity variation of ARs, we have made use of the advantageous positioning of the STEREO and SOHO spacecraft to track and characterize the white-light ejecta of a long-duration AR during its complete lifetime (spanning approximately 124 days). We found a large number of mass ejections (108), distributed non-uniformly in time, i.e. 56% of all CMEs occurred in 16% of the AR lifetime. Motivated by the large number and clustering of the CMEs within the studied

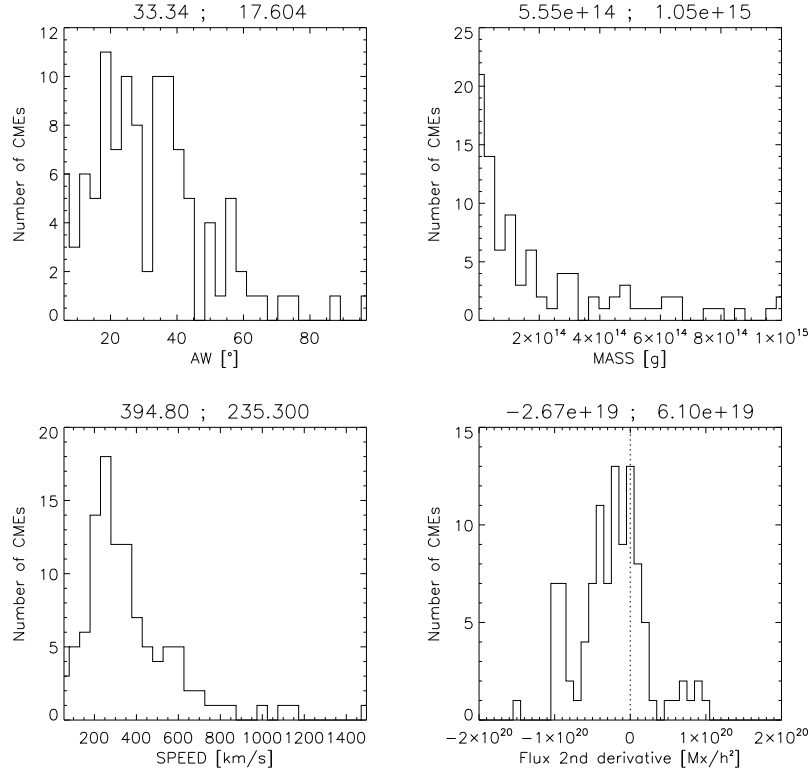


Figure 3: Distribution of the AW , mass, speed and value of the magnetic flux second derivative during onset (see axes labels) for the 108 identified CMEs. The title in each panel presents the average and standard error, respectively. Further details are described in the text.

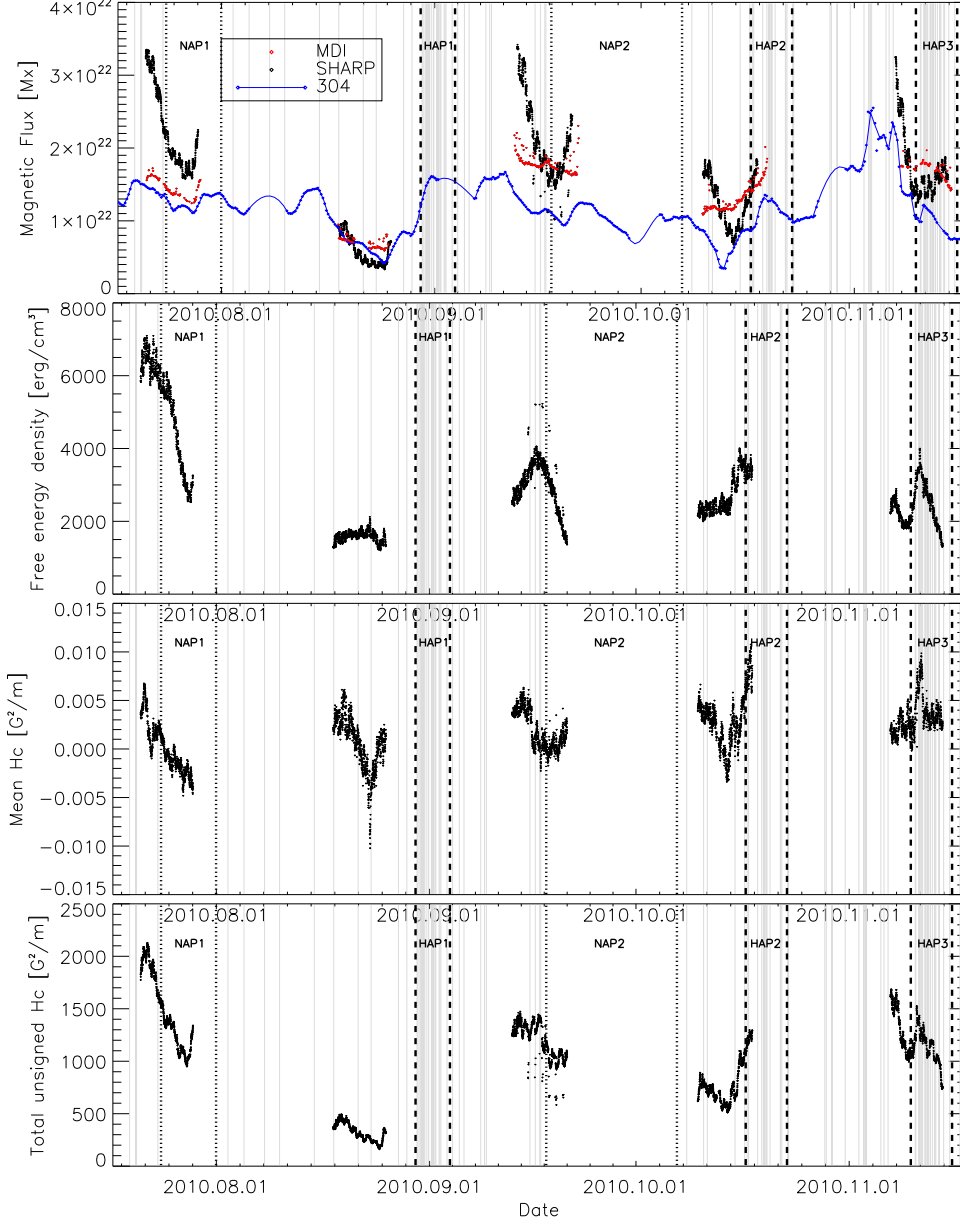


Figure 4: Time evolution of SHARP photospheric magnetic field parameters. From top to bottom we show the magnetic flux estimated via three different sources (see legend and Sect. 2.1), a proxy for the free magnetic energy density, the mean current helicity H_c and the total unsigned H_c . The vertical lines have the same meaning than in Fig. 2.

time interval, we focus the discussion below on comparing the occurrence of full ejective activity periods with the GOES X-ray flaring activity, and the long-term (multi-day, see [Green et al. 2018](#)) temporal variation of the AR photospheric properties using SDO and STEREO. Such analysis differs from the more frequent studies of the short-term (tens of hours) evolution of the AR magnetic properties, preceding the occurrence of single (or few) CMEs and/or flares (see Sect. 1).

Fig. 4 shows that HAP1 and HAP2 take place during or after periods of persistent (≈ 3 days) magnetic flux increments. Using the 304 Å proxy these increments are of $\approx 1.2 \times 10^{22}$ and $\approx 1 \times 10^{22}$ Mx for HAP1 and HAP2, respectively. Moreover, it stands out that a large portion of the CMEs were ejected when the flux variation was decreasing, i.e. reaching a plateau. The bottom-right histogram presented in Fig. 3 quantifies this, showing that 73 out of 108 CMEs occur when the second temporal derivative of the magnetic flux is negative. Note that the number of events analyzed is small and only a proxy of the magnetic flux is used, thus a hard conclusion from these results cannot be drawn. However, many other single or few-events studies report CMEs occurring after the flux emergence, e.g. [Romano et al. 2014](#); [Bobra et al. 2014](#); [Li et al. 2012](#); [Mandrini et al. 2014](#); [Jiang et al. 2014](#). This is likely related to the fact that the non-potential energy may continue increasing during the flux stabilization period, as the shearing photospheric motions twist the emerged flux rope building up the coronal field helicity. During HAP2, the flux emergence is also followed by a clear increase of the field non-potentiality before the burst of several CMEs, suggesting again the twisted flux emergence and its accompanying shearing photospheric motions as the main free energy contributors. This is manifested by the jumps in the magnetic free energy density ($\approx 2000 \text{ erg cm}^{-3}$), mean Hc ($\approx 0.012 \text{ G}^2 \text{ m}^{-1}$) and total unsigned Hc ($\approx 700 \text{ G}^2 \text{ m}^{-1}$), see Fig. 4.

The case of HAP3 is different in that it starts during the decay phase of AR 11121. A persistent decrease (≈ 5 days) of the total unsigned magnetic flux is registered before HAP3 begins (according to the SHARP data and the 304 Å proxy) and continues with only moderate increases and recurrent dips ($< 5 \times 10^{21}$ Mx, according to the SHARP data) until the end of the period. During the decay phase of bipolar ARs, the CME activity can increase due to the flux cancellations produced at the PIL or by the motion of magnetic elements ([van Driel-Gesztelyi and Green, 2015](#)), which induce the successive formation and eruption of flux ropes (because it favors the onset of torus instabilities [Forbes and Isenberg 1991](#), among others). However, for the case

of HAP3, the persistent increase in the free magnetic energy density and Hc (for a ≈ 3 days period and similar in value to the ones registered before HAP2, see Fig. 4) are most likely related to the emergence of AR 11123, from which most of the EUV brightenings in HAP3 originate (see Fig. 1). As detailed by [Mandrini et al. \(2014\)](#), a series of fast bipolar emergences formed AR 11123 between 9 and 10 November. This produced an increase in AR 11123 flux (partially masked in Fig 4 because we consider the full AR complex including AR 11121, see Fig. 5 in [Mandrini et al. 2014](#)) due to the creation and subsequent topological evolution of the magnetic field in the following two days. After this period, the free energy density and the mean Hc peak, suggesting that the non-potential energy was built by photospheric shearing motions, and the most active portion of HAP3 begins. Note that, during most of HAP3 the free magnetic energy density reduces monotonically due to the successive CMEs.

We note that, even though HAP1 and HAP2 were preceded by a flux increment and occurred when the AR was a simple bipole, the aggregate CME properties reported in Table 2 do not substantially differ from those of HAP3, which occurred after a strong flux decrease when AR11123 emerged and the photospheric field was a more complex quadrupole (two bipoles).

Substantial X-ray flaring activity was registered during HAP2 and HAP3 (54 flares), however only 40% (6 out of 15) of CMEs in HAP2 were associated to a flare. This association increases to 71% (17 out of 24) for HAP3, which includes CMEs that are on average 52% faster and 81% more massive, see Table 2. This is in agreement with the well known fact that more energetic CMEs tend to be preceded by bigger flares, see e.g. [Webb and Howard \(2012\)](#) and references therein. On the other hand, 98% of the flares registered during the AR lifetime are of B or C class, and most of the CMEs are slow (75% having speeds $< 600 \text{ km s}^{-1}$). Moreover, no X-class flare was associated to the AR, although the fastest 4 CMEs, within the speed range commonly associated to X-class flares ($\approx 1500 \text{ km s}^{-1}$, see [Yashiro et al., 2005](#)), were produced during the back-side transit in HAP1, not visible by GOES.

The two main periods of no ejective activity, NAP1 and NAP2, begin during a phase of strong reduction of the free magnetic energy density, although the initial values are comparable to those found at the beginning of HAP2 and HAP3. NAP1 also starts during a period of Hc and flux reduction, suggesting that the non-potential energy was reduced by flux cancellation, likely related to the decay of the small western bipole present during the first rotation of AR11089 (see top-left panel in Fig. 1). Such a flux cancellation is

accompanied by flaring reconnections (see Table 2), however, no CMEs are observed. This can be due to the fact that the AR is young and thus no well formed flux ropes are present and/or due to a more efficient confinement by the overlying strapping field, see e.g. Romano et al. (2014). On the other hand, NAP2 begins with a flux rise (according to SHARP data) and not a marked Hc increment, suggesting a mechanism other than flux cancellation, diffusion, or field ejection to explain the free energy reduction, e.g. flux emergence with an helicity sign opposite to the predominant. The main results of the long-term, multi-viewpoint study reported here are summarized below:

- 56% of the 108 CMEs identified occur in three activity periods (HAP1, HAP2 and HAP3) spanning 16% of the AR life time (≈ 124 days). Two periods of no CME activity were identified (NAP1 and NAP2) spanning 23% of the AR life time.
- HAP1 and HAP2 take place after periods of persistent (≈ 3 days) magnetic flux increment ($\approx 1 \times 10^{22}$ Mx) and free magnetic energy (only measurable for HAP2).
- 73 out of 108 CMEs occur when the flux change rate is decreasing, i.e. during intervals of negative second time derivative.
- HAP3 occurs during the decay phase of the AR 11123 and a persistent reduction (≈ 5 days) of the magnetic flux. The high CME activity is related to the free energy increment produced by the flux injection and photospheric motions induced by the emergence of AR 11121.
- There is no statistical difference among the aggregate CME properties of the three activity periods.
- 62 CMEs occurred during front-side transits, 33 were associated to one of the 162 GOES flares identified. The more energetic the flare, the higher the association rate, i.e. 10% (13 out of 127), 55% (17 out of 31), 75% (3 out of 4) of class B, C and M, respectively.
- Most of the CMEs found are slow (75 % having speeds $< 600 \text{ km}^{-1}$) and thus 98% of the flares are of B and C class.
- NAP1 and NAP2 occur during phases of strong reduction of free magnetic energy. NAP1 occur during a flux reduction interval accompanied

by flaring activity but no CMEs, likely because the AR was young and no sizable filamentary structure was present.

- No obvious correlation was found between the long-term variation of the average photospheric properties, and the values of the aggregated CME characteristics of the high activity periods.

Regarding the last point, it is known that the photospheric field properties are only a partial indication of the likelihood of an AR to produce a mass ejection, see e.g. [Green et al. \(2018\)](#); [Mandrini et al. \(2014b\)](#); [Romano et al. \(2014\)](#). The characteristics of the higher coronal field above the potential CME source region, e.g. the presence of streamers, are not addressed here and strongly affect the CME production and early kinematics. An additional effect, that we plan to further study, is related to the fact that we employ photospheric quantities averaged over the full SHARP patch, while the EUV brightenings associated to the CMEs tend to cluster in specific sectors within the AR.

Acknowledgements: HC, CHM and MLF are members of the Carrera del Investigador Científico (CONICET). FAI and FML are fellows of CONICET. LM acknowledges a scholarship from UTN and from the CIN. The authors appreciate financial support from the Argentine grants PICT 2012-973 (AN-PCyT) and PIP 2012-01-403 (CONICET). FAI, HC, LM, and FML thank support from project UTN UTI4035TC and UTI4915TC. IUU acknowledges support by a grant from the NASA Heliophysics Guest Investigator program (NNH16AC71I). The authors acknowledge the use of data from the STEREO (NASA), SDO (NASA), and SOHO (ESA/NASA) missions. These data are produced by the AIA, HMI, SECCHI, LASCO, and MDI international consortia.

References

- Abbo, L., Ofman, L., Antiochos, S. K., Hansteen, V. H., Harra, L., Ko, Y.-K., Lapenta, G., Li, B., Riley, P., Strachan, L., von Steiger, R. and Wang, Y.-M. (2016), ‘Slow Solar Wind: Observations and Modeling’, *Space Sci. Rev.* **201**, 55–108.
- Amari, T., Luciani, J. F., Mikic, Z. and Linker, J. (2000), ‘A Twisted Flux Rope Model for Coronal Mass Ejections and Two-Ribbon Flares’, *ApJ* **529**, L49–L52.

- Antiochos, S. K., DeVore, C. R. and Klimchuk, J. A. (1999), ‘A Model for Solar Coronal Mass Ejections’, *ApJ* **510**, 485–493.
- Aulanier, G., Török, T., Démoulin, P. and DeLuca, E. E. (2010), ‘Formation of Torus-Unstable Flux Ropes and Electric Currents in Erupting Sigmoids’, *ApJ* **708**, 314–333.
- Billings, D. E. (1966), *A guide to the solar corona*, Elsevier Science, New York.
- Bobra, M. G., Sun, X., Hoeksema, J. T., Turmon, M., Liu, Y., Hayashi, K., Barnes, G. and Leka, K. D. (2014), ‘The Helioseismic and Magnetic Imager (HMI) Vector Magnetic Field Pipeline: SHARPs - Space-Weather HMI Active Region Patches’, *Sol. Phys.* **289**, 3549–3578.
- Bothmer, V. and Daglis, I. A. (2007), *Space Weather: Physics and Effects*, Environmental Sciences, Springer-Verlag Berlin Heidelberg.
- Brueckner, G. E., Howard, R. A., Koomen, M. J., Korendyke, C. M., Michels, D. J., Moses, J. D., Socker, D. G., Dere, K. P., Lamy, P. L., Llebaria, A., Bout, M. V., Schwenn, R., Simnett, G. M., Bedford, D. K. and Eyles, C. J. (1995), ‘The Large Angle Spectroscopic Coronagraph (LASCO)’, *Sol. Phys.* **162**, 357–402.
- Canfield, R. C., Hudson, H. S. and McKenzie, D. E. (1999), ‘Sigmoidal morphology and eruptive solar activity’, *Geophys. Res. Lett.* **26**, 627–630.
- Chandra, R., Mandrini, C. H., Schmieder, B., Joshi, B., Cristiani, G. D., Cremades, H., Pariat, E., Nuevo, F. A., Srivastava, A. K. and Uddin, W. (2017), ‘Blowout jets and impulsive eruptive flares in a bald-patch topology’, *A&A* **598**, A41.
- Chandra, R., Schmieder, B., Mandrini, C. H., Démoulin, P., Pariat, E., Török, T. and Uddin, W. (2011), ‘Homologous Flares and Magnetic Field Topology in Active Region NOAA 10501 on 20 November 2003’, *Sol. Phys.* **269**, 83–104.
- Chen, J., Howard, R. A., Brueckner, G. E., Santoro, R., Krall, J., Paswaters, S. E., St. Cyr, O. C., Schwenn, R., Lamy, P. and Simnett, G. M. (1997), ‘Evidence of an Erupting Magnetic Flux Rope: LASCO Coronal Mass Ejection of 1997 April 13’, *ApJ* **490**, L191–L194.

- Chen, P. F. (2011), ‘Coronal mass ejections: Models and their observational basis’, *Living Reviews in Solar Physics* **8**(1), 1.
URL: <https://doi.org/10.12942/lrsp-2011-1>
- Chertok, I., V. Grechnev, V. and Abunin, A. (2019), An early diagnostics of the geoeffectiveness of solar eruptions from photospheric magnetic flux observations: The transition from soho to sdo, *in* J. Zhang, X. Blanco-Cano, N. Nitta, N. Srivastava and C. H. Mandrini, eds, ‘Earth-affecting Solar Transients’, Springer Netherlands, pp. 729–744.
- Colaninno, R. C. and Vourlidas, A. (2009), ‘First Determination of the True Mass of Coronal Mass Ejections: A Novel Approach to Using the Two STEREO Viewpoints’, *ApJ* **698**, 852–858.
- Cremades, H., Mandrini, C. H., Schmieder, B. and Crescitelli, A. M. (2015), ‘Coronal Mass Ejections from the Same Active Region Cluster: Two Different Perspectives’, *Sol. Phys.* **290**, 1671–1686.
- Démoulin, P., Mandrini, C. H., van Driel-Gesztelyi, L., Thompson, B. J., Plunkett, S., Kovári, Z., Aulanier, G. and Young, A. (2002), ‘What is the source of the magnetic helicity shed by CMEs? The long-term helicity budget of AR 7978’, *A&A* **382**, 650–665.
- Domingo, V., Fleck, B. and Poland, A. I. (1995), ‘The SOHO mission: An overview’, *Sol. Phys.* **162**, 1–37.
- Falconer, D. A., Moore, R. L. and Gary, G. A. (2006), ‘Magnetic Causes of Solar Coronal Mass Ejections: Dominance of the Free Magnetic Energy over the Magnetic Twist Alone’, *ApJ* **644**, 1258–1272.
- Fludra, A. and Ireland, J. (2008), ‘Radiative and magnetic properties of solar active regions. I. Global magnetic field and EUV line intensities’, *A&A* **483**(2), 609–621.
- Forbes, T. G. and Isenberg, P. A. (1991), ‘A catastrophe mechanism for coronal mass ejections’, *ApJ* **373**, 294–307.
- Forbes, T. G., Seaton, D. B. and Reeves, K. K. (2018), ‘Reconnection in the post-impulsive phase of solar flares’, *The Astrophysical Journal* **858**(2), 70.
URL: <https://doi.org/10.3847/2F1538-4357/2Faabad4>

- Gopalswamy, N. (2010), Coronal Mass Ejections: a Summary of Recent Results, *in* I. Dorotovic, ed., ‘20th National Solar Physics Meeting’, Slovak Central Observatory, Hurbanovo, Slovakia, pp. 108–130.
- Gopalswamy, N., Lara, A., Yashiro, S., Nunes, S. and Howard, R. A. (2003), Coronal mass ejection activity during solar cycle 23, *in* A. Wilson, ed., ‘Solar Variability as an Input to the Earth’s Environment’, Vol. 535 of *ESA Special Publication*, pp. 403–414.
- Green, L. M., Démoulin, P., Mandrini, C. H. and Van Driel-Gesztelyi, L. (2003), ‘How are Emerging Flux, Flares and CMEs Related to Magnetic Polarity Imbalance in MDI Data?’, *Sol. Phys.* **215**, 307–325.
- Green, L. M., López fuentes, M. C., Mandrini, C. H., Démoulin, P., Van Driel-Gesztelyi, L. and Culhane, J. L. (2002), ‘The Magnetic Helicity Budget of a cme-Prolific Active Region’, *Sol. Phys.* **208**, 43–68.
- Green, L. M., Török, T., Vršnak, B., Manchester, W. and Veronig, A. (2018), ‘The Origin, Early Evolution and Predictability of Solar Eruptions’, *Space Sci. Rev.* **214**, 46.
- Guo, Y., Démoulin, P., Schmieder, B., Ding, M. D., Vargas Domínguez, S. and Liu, Y. (2013), ‘Recurrent coronal jets induced by repetitively accumulated electric currents’, *A&A* **555**, A19.
- Harra, L. K., Ugarte-Urra, I., De Rosa, M., Mandrini, C., van Driel-Gesztelyi, L., Baker, D., Culhane, J. L. and Démoulin, P. (2017), ‘A study of the long term evolution in active region upflows’, *PASJ* **69**, 47.
- Hood, A. W., Archontis, V., Galsgaard, K. and Moreno-Insertis, F. (2009), ‘The emergence of toroidal flux tubes from beneath the solar photosphere’, *A&A* **503**, 999–1011.
- Howard, R. A., Moses, J. D., Vourlidas, A., Newmark, J. S., Socker, D. G., Plunkett, S. P., Korendyke, C. M., Cook, J. W., Hurley, A., Davila, J. M. and et al. (2008), ‘Sun Earth Connection Coronal and Heliospheric Investigation (SECCHI)’, *Space Sci. Rev.* **136**, 67–115.
- Jiang, C., Wu, S. T., Feng, X. and Hu, Q. (2014), ‘Formation and Eruption of an Active Region Sigmoid. I. A Study by Nonlinear Force-free Field Modeling’, *ApJ* **780**, 55.

- Kaiser, M. L., Kucera, T. A., Davila, J. M., St. Cyr, O. C., Guhathakurta, M. and Christian, E. (2008), ‘The STEREO mission: An introduction’, *Space Sci. Rev.* **136**, 5–16.
- Kliem, B., Lin, J., Forbes, T. G., Priest, E. R. and Török, T. (2014), ‘Catastrophe versus Instability for the Eruption of a Toroidal Solar Magnetic Flux Rope’, *ApJ* **789**, 46.
- Kliem, B. and Török, T. (2006), ‘Torus instability’, *Phys. Rev. Lett.* **96**, 255002.
URL: <https://link.aps.org/doi/10.1103/PhysRevLett.96.255002>
- Ko, Y.-K., Young, P. R., Muglach, K., Warren, H. P. and Ugarte-Urra, I. (2016), ‘Correlation of Coronal Plasma Properties and Solar Magnetic Field in a Decaying Active Region’, *ApJ* **826**, 126.
- Koleva, K., Madjarska, M. S., Duchlev, P., Schrijver, C. J., Vial, J. C., Buchlin, E. and Dechev, M. (2012), ‘Kinematics and helicity evolution of a loop-like eruptive prominence’, *A&A* **540**, A127.
- Lara, A., Gopalswamy, N., Xie, H., Mendoza-Torres, E., Pérez-Erriquez, R. and Michalek, G. (2006), ‘Are halo coronal mass ejections special events?’, *J. Geophys. Res. (Space Physics)* **111**, 6107.
- Lemen, J. R., Title, A. M., Akin, D. J., Boerner, P. F., Chou, C., Drake, J. F., Duncan, D. W., Edwards, C. G., Friedlaender, F. M., Heyman, G. F. and et al. (2012), ‘The Atmospheric Imaging Assembly (AIA) on the Solar Dynamics Observatory (SDO)’, *Sol. Phys.* **275**, 17–40.
- Li, L. P., Zhang, J., Li, T., Yang, S. H. and Zhang, Y. Z. (2012), ‘Study of the first productive active region in solar cycle 24’, *A&A* **539**, A7.
- Lin, J., Raymond, J. C. and van Ballegooijen, A. A. (2004), ‘The Role of Magnetic Reconnection in the Observable Features of Solar Eruptions’, *ApJ* **602**, 422–435.
- Liu, C., Deng, N., Liu, R., Lee, J., Wiegmann, T., Jing, J., Xu, Y., Wang, S. and Wang, H. (2012), ‘Rapid Changes of Photospheric Magnetic Field after Tether-cutting Reconnection and Magnetic Implosion’, *ApJL* **745**, L4.

- Liu, L., Wang, Y., Wang, J., Shen, C., Ye, P., Liu, R., Chen, J., Zhang, Q. and Wang, S. (2016), ‘Why is a Flare-rich Active Region CME-poor?’, *ApJ* **826**, 119.
- Liu, Y., Hoeksema, J. T., Scherrer, P. H., Schou, J., Couvidat, S., Bush, R. I., Duvall, T. L., Hayashi, K., Sun, X. and Zhao, X. (2012b), ‘Comparison of Line-of-Sight Magnetograms Taken by the Solar Dynamics Observatory/Helioseismic and Magnetic Imager and Solar and Heliospheric Observatory/Michelson Doppler Imager’, *Sol. Phys.* **279**, 295–316.
- López, F. M., Hebe Cremades, M., Nuevo, F. A., Balmaceda, L. A. and Vásquez, A. M. (2017), ‘Mass-Loss Evolution in the EUV Low Corona from SDO/AIA Data’, *Sol. Phys.* **292**(1), 6.
- MacTaggart, D. and Hood, A. W. (2010), ‘SIMULATING THE “SLIDING DOORS” EFFECT THROUGH MAGNETIC FLUX EMERGENCE’, *The Astrophysical Journal* **716**(2), L219–L222.
URL: <https://doi.org/10.1088%2F2041-8205%2F716%2F2%2F1219>
- Manchester, W. B., Gombosi, T. I., Roussev, I., de Zeeuw, D. L., Sokolov, I. V., Powell, K. G., Tóth, G. and Opher, M. (2004), ‘Three-dimensional MHD simulation of a flux rope driven CME’, *J. Geophys. Res. (Space Physics)* **109**, 1102.
- Mandrini, C. H., Demoulin, P., Schmieder, B., Deluca, E. E., Pariat, E. and Uddin, W. (2006), ‘Companion Event and Precursor of the X17 Flare on 28 October 2003’, *Sol. Phys.* **238**, 293–312.
- Mandrini, C. H., Démoulin, P., van Driel-Gesztelyi, L., Green, L. M. and López Fuentes, M. C. (2004), ‘Magnetic Helicity Budget of Solar-Active Regions from the Photosphere to Magnetic Clouds’, *Ap&SS* **290**, 319–344.
- Mandrini, C. H., Nuevo, F. A., Vásquez, A. M., Démoulin, P., van Driel-Gesztelyi, L., Baker, D., Culhane, J. L., Cristiani, G. D. and Pick, M. (2014b), ‘How Can Active Region Plasma Escape into the Solar Wind from Below a Closed Helmet Streamer?’, *Sol. Phys.* **289**, 4151–4171.
- Mandrini, C. H., Schmieder, B., Démoulin, P., Guo, Y. and Cristiani, G. D. (2014), ‘Topological analysis of emerging bipole clusters producing violent solar events’, *Sol. Phys.* **289**, 2041–2071.

- McKenzie, D. E. and Canfield, R. C. (2008), ‘Hinode XRT observations of a long-lasting coronal sigmoid’, *A&A* **481**, L65–L68.
- Moore, R. L. and Roumeliotis, G. (1992), Triggering of Eruptive Flares - Destabilization of the Preflare Magnetic Field Configuration, *in* Z. Svestka, B. V. Jackson and M. E. Machado, eds, ‘IAU Colloq. 133: Eruptive Solar Flares’, Vol. 399 of *Lecture Notes in Physics*, Berlin Springer Verlag, pp. 69–78.
- Moore, R. L., Sterling, A. C., Hudson, H. S. and Lemen, J. R. (2001), ‘Onset of the magnetic explosion in solar flares and coronal mass ejections’, *The Astrophysical Journal* **552**(2), 833–848.
URL: <https://doi.org/10.1086%2F320559>
- Murray, S. A., Guerra, J. A., Zucca, P., Park, S.-H., Carley, E. P., Gallagher, P. T., Vilmer, N. and Bothmer, V. (2018), ‘Connecting coronal mass ejections to their solar active region sources: Combining results from the helcats and flarecast projects’, *Solar Physics* **293**(4), 60.
URL: <https://doi.org/10.1007/s11207-018-1287-4>
- Pesnell, W. D., Thompson, B. J. and Chamberlin, P. C. (2012), ‘The Solar Dynamics Observatory (SDO)’, *Sol. Phys.* **275**, 3–15.
- Petrie, G. J. D. (2013), ‘Solar Magnetic Activity Cycles, Coronal Potential Field Models and Eruption Rates’, *ApJ* **768**, 162.
- Pluta, A., Mrotzek, N., Vourlidas, A., Bothmer, V. and Savani, N. (2019), ‘Combined geometrical modelling and white-light mass determination of coronal mass ejections’, *A&A* **623**, A139.
- Poisson, M., López Fuentes, M., Mandrini, C. H. and Démoulin, P. (2015b), ‘Active-Region Twist Derived from Magnetic Tongues and Linear Force-Free Extrapolations’, *Sol. Phys.* **290**, 3279–3294.
- Poisson, M., Mandrini, C. H., Démoulin, P. and López Fuentes, M. (2015a), ‘Evidence of Twisted Flux-Tube Emergence in Active Regions’, *Sol. Phys.* **290**, 727–751.
- Priest, E. and Forbes, T. (2002), ‘The magnetic nature of solar flares’, *The Astronomy and Astrophysics Review* **10**(4), 313–377.
URL: <https://doi.org/10.1007/s001590100013>

- Riley, P., Schatzman, C., Cane, H. V., Richardson, I. G. and Gopalswamy, N. (2006), ‘On the Rates of Coronal Mass Ejections: Remote Solar and In Situ Observations’, *ApJ* **647**, 648–653.
- Robbrecht, E. and Berghmans, D. (2004), ‘Automated recognition of coronal mass ejections (CMEs) in near-real-time data’, *A&A* **425**, 1097–1106.
- Romano, P., Zuccarello, F. P., Guglielmino, S. L. and Zuccarello, F. (2014), ‘Evolution of the Magnetic Helicity Flux during the Formation and Eruption of Flux Ropes’, *ApJ* **794**, 118.
- Rust, D. M. and Kumar, A. (1996), ‘Evidence for Helically Kinked Magnetic Flux Ropes in Solar Eruptions’, *ApJL* **464**, L199–L202.
- Scherrer, P. H., Bogart, R. S., Bush, R. I., Hoeksema, J. T., Kosovichev, A. G., Schou, J., Rosenberg, W., Springer, L., Tarbell, T. D., Title, A., Wolfson, C. J., Zayer, I. and MDI Engineering Team (1995), ‘The Solar Oscillations Investigation - Michelson Doppler Imager’, *Sol. Phys.* **162**, 129–188.
- Scherrer, P. H., Schou, J., Bush, R. I., Kosovichev, A. G., Bogart, R. S., Hoeksema, J. T., Liu, Y., Duvall, T. L., Zhao, J., Title, A. M., Schrijver, C. J., Tarbell, T. D. and Tomczyk, S. (2012), ‘The Helioseismic and Magnetic Imager (HMI) Investigation for the Solar Dynamics Observatory (SDO)’, *Sol. Phys.* **275**, 207–227.
- Schrijver, C. J. (1987), ‘Solar active regions - Radiative intensities and large-scale parameters of the magnetic field’, *A&A* **180**, 241–252.
- Schrijver, C. J., Aulanier, G., Title, A. M., Pariat, E. and Delannée, C. (2011), ‘THE 2011 FEBRUARY 15 x2 FLARE, RIBBONS, CORONAL FRONT, AND MASS EJECTION: INTERPRETING THE THREE-DIMENSIONAL VIEWS FROM THE SOLAR DYNAMICS OBSERVATORY AND STEREO GUIDED BY MAGNETOHYDRODYNAMIC FLUX-ROPE MODELING’, *The Astrophysical Journal* **738**(2), 167.
- Török, T. and Kliem, B. (2005), ‘Confined and Ejective Eruptions of Kink-unstable Flux Ropes’, *ApJL* **630**, L97–L100.

- Ugarte-Urra, I., Upton, L. and Warren, H. (2018), He II 304 Å proxy for magnetic field properties in far-side complex topologies, *in* ‘AGU Fall Meeting Abstracts’, Vol. 2018, pp. SH41C–3655.
- Ugarte-Urra, I., Upton, L., Warren, H. P. and Hathaway, D. H. (2015), ‘Magnetic Flux Transport and the Long-term Evolution of Solar Active Regions’, *ApJ* **815**, 90.
- van Driel-Gesztelyi, L. and Green, L. (2015), ‘Evolution of active regions’, *Living Rev. Sol. Phys.* **12**:1.
- Vourlidas, A., Howard, R. A., Esfandiari, E., Patsourakos, S., Yashiro, S. and Michalek, G. (2010), ‘Comprehensive Analysis of Coronal Mass Ejection Mass and Energy Properties Over a Full Solar Cycle’, *ApJ* **722**, 1522–1538.
- Vourlidas, A., Lynch, B. J., Howard, R. A. and Li, Y. (2013), ‘How many CMEs have flux ropes? Deciphering the signatures of shocks, flux ropes, and prominences in coronagraph observations of CMEs’, *Sol. Phys.* **284**, 179–201.
- Wang, Y. and Zhang, J. (2008), ‘A Statistical Study of Solar Active Regions That Produce Extremely Fast Coronal Mass Ejections’, *ApJ* **680**, 1516–1522.
- Webb, D. F. and Howard, T. A. (2012), ‘Coronal mass ejections: Observations’, *Living Rev. Solar Phys.* **9**(3).
URL: <http://www.livingreviews.org/lrsp-2012-3>
- Yashiro, S., Gopalswamy, N., Akiyama, S., Michalek, G. and Howard, R. A. (2005), ‘Visibility of coronal mass ejections as a function of flare location and intensity’, *Journal of Geophysical Research (Space Physics)* **110**, A12S05.
- Yashiro, S., Gopalswamy, N., Michalek, G., St. Cyr, O. C., Plunkett, S. P., Rich, N. B. and Howard, R. A. (2004), ‘A catalog of white light coronal mass ejections observed by the SOHO spacecraft’, *J. Geophys. Res. (Space Physics)* **109**, 7105.
- Zangrilli, L. and Poletto, G. (2016), ‘Evolution of active region outflows throughout an active region lifetime’, *A&A* **594**, A40.

- Zhang, J., Blanco-Cano, X., Nitta, N., Srivastava, N. and Mandrini, C. H. (2018), ‘Editorial: Earth-affecting Solar Transients’, *Sol. Phys.* **293**, 80.
- Zuccarello, F., Guglielmino, S. L. and Romano, P. (2014), ‘Evolution and Dynamics of Orphan Penumbrae in the Solar Photosphere: Analysis from Multi-instrument Observations’, *ApJ* **787**, 57.

